Impact interaction of in-flight high-energy molten volcanic ash droplets with jet engines

Wenjia Song [a,b] [*], Shanjie Yang [a,c], Masahiro Fukumoto [d], Yan Lavallée [e], Siddharth Lokachari [a], Hongbo Guo [c], Yancheng You [b] [*], Donald B. Dingwell [a]

[a] Department of Earth and Environmental Sciences, Ludwig-Maximilians Universität München, Theresienstrasse 41, 80333 Munich, Germany

[b] School of Aerospace Engineering, Xiamen University, 361102 Xiamen, China

[c] School of Materials Science and Engineering, Beihang University, 100191 Beijing, China

[d] Department of Mechanical Engineering, Toyohashi University of Technology, 1-1 Tempaku-cho, 441-8580 Toyohashi, Japan

[e] Department of Earth, Ocean and Ecological Sciences, University of Liverpool, Liverpool L69 3GP, UK

*Corresponding authors:

Wenjia Song, Department of Earth and Environmental Sciences, Ludwig-Maximilians-Universität (LMU), Theresienstrasse 41, 80333 Munich, Germany. (wenjia.song@lmu.de)
Telephone: +49 (0) 89 2180 4293

Yancheng You, School of Aerospace Engineering, Xiamen University, 361102 Xiamen, China. (yancheng.you@xmu.edu.cn)
Telephone: +86 (0) 592 2186 849

1

Abstract

The turbine technology incorporated in jet engines is inherently vulnerable to attack by environmental silicate debris. Amongst the various kinds of such debris, volcanic ash is a particular threat as its glass softens to a liquid at temperatures of 500-800°C, far below jet engine operating temperatures of ~ 1500 ºC. As a result, ingested re-molten droplets impact and form splats on the protective thermal barrier coatings (TBCs). Investigation of the damage to jet engines ensuing from this process has, to date been restricted to forensic observations after critical encounters. Here, we employ a thermal spray technology to recreate the '*in-situ*' generation of molten volcanic ash droplets and observe their morphological evolution and interaction with TBCs. The mechanism of splat formation is found to depend both on substrate topography and on in-flight droplet characteristics, whereby splat circularity increases with surface roughness and with the product of the Weber and Reynolds numbers. The experiments reveal that the molten ash droplet adhesion rate is dictated by droplet temperature and viscosity, ash concentration and substrate roughness. A new dimensionless number, *S*, is developed to quantify the molten ash droplet adhesion rate to both substrate topography and in-flight droplet characteristics. These findings provide a greatly improved basis for the quantification of the hazard potential of volcanic ash to jet engines and should be incorporated into protocols for operational aviation response during volcanic crises.

Keywords: Thermal barrier coatings, volcanic ash, jet engines, impact.

1. Introduction

Volcanic ash poses a critical risk to aviation safety [1-4]. Since 1953, over 130 jet aircraft have inadvertently encountered volcanic ash clouds and suffered, as a result, varying degrees of damage, endangering in the process the lives of tens of thousands of passengers [5,6]. The 2010 eruption of Eyjafjallajökull volcano in Iceland (Fig.1a) lead to the most severe air-traffic disruption since World War II and the operational response was responsible for major economic losses approaching around 1.7 billion [7].
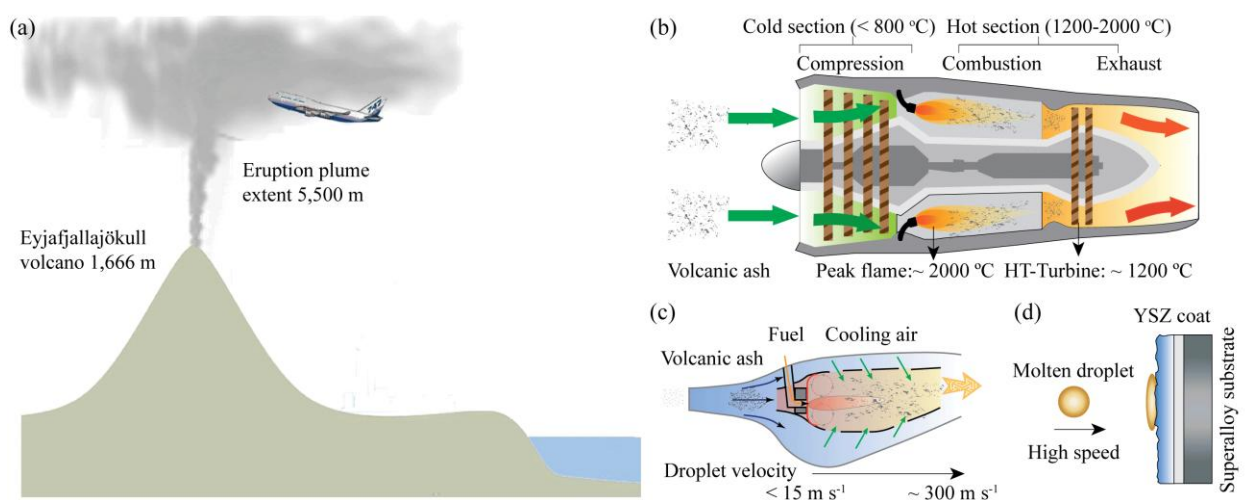

Fig. 1. Impact of volcanic ash to aviation safety. (**a**) Schematic of volcanic ash hazards from the 2010 eruption of Eyjafjallajökull volcano in Iceland on aviation. (**b**) Jet engine volcanic ash ingestion, including (**c**) melting of volcanic ash in the combustor and (**d**) the interaction of high-energy molten droplet impacts with TBCs.

The primary threat of volcanic ash to jet engines involves the impact and interaction of very fine (≤ 63 μm), high-energy molten volcanic ash droplets (e.g., temperature: $1200 \leq 1500$ $^{\circ}$C and velocity: $100 \leq 300$ m s^{-1}) - formed by rapidly softening and melting volcanic ash solid particles passing through the hot-section airfoils of jet engines' combustion region [8]. In detail, volcanic ash particles, with glass transition temperatures in the range of 500-800 $^{\circ}$C [9], yield molten droplets of variable viscosity upon exposure to the operating combustion chamber (peak flame temperature: ~2000 $^{\circ}$C, Fig. 1b) [10]. These molten droplets are then carried by the hot gas stream out of the engine combustion chamber whereby they are accelerated from low speeds (~15 m s^{-1}) up to near-supersonic speeds (~300 m s^{-1}) (Fig. 1c) as they enter the hot-section airfoils (i.e., the first stage of the high-pressure turbine, consisting of a row of

3

stationary nozzle guide vanes and one row of moving turbine blades) [11,12]. During transport through the hot-section airfoils, the molten droplets can impact upon and adhere to the surfaces of hot-section airfoils operating at high temperatures (~1200 ºC). Adhering droplets form so-called "splats" (Fig. 1d) [13].

Even in situations where only a few molten silicate ash droplets adhere to the surface of hot-section airfoils, an initial deposit layer can form and large melt pockets (several cubic centimeters in volume) can accumulate [14]. Such deposits can 1) block cooling traps and air flow paths, and 2) react with the top coating of the hot-section airfoils; i.e., the protective ceramic thermal barrier coatings (TBCs) [15,16]. The TBCs consist of a top ceramic layer and a middle metallic bond coat with a thermally grown oxide (TGO) formed by reaction with the combustion gas, which provides thermal insulation to the underlying Ni-based superalloys of turbine components [17]. The top ceramic coating is made of tetragonal-phase ZrO_2 ceramic stabilized by 7 wt. % Y_2O_3 (commonly referred to as 7YSZ) [18]. The 7YSZ coatings typically used in stationary parts of jet engines (i.e., combustor and nozzle guide vanes) are deposited by atmospheric plasma-spraying (APS) to form a very fine lamellar microstructure with a low thermal conductivity [19]. In contrast, the coatings applied to rotating components of aero-turbines (i.e., turbine blades), which are subject to frequent thermal stressing cycles (during take-off and landing) are deposited by electron beam physical vapour deposition (EB-PVD) to create a feathery microstructure of columnar grains for an enhanced stress tolerance [20]. At high temperature, the molten low-viscosity ash droplets infiltrate small open capillaries in the top layer of a TBCs system, causing spallation of this coating that deteriorates engine performance [21,22] to the point of catastrophic failure [23].

Mitigating the impact of volcanic ash in jet engines has been the subject of numerous studies in recent decades. There is, in particular, significant interest in constraining the impact process of volcanic ash in jet engines from large-scale analyses of application-ready engine operations in volcanic ash-laden

4

environments [24,25] to lab-scale test based on the ingestion of volcanic ash into small turbojet engines [26,27]. Recent advances provided by thermal spray technologies have allowed the simulation of molten volcanic ash droplets impact on turbine blades, helping to constrain the factors controlling the likelihood of ash adhesion in jet engines [28-31]. Despite widespread efforts to explore the threshold of adhesion vs rebound threshold during impact, the processes by which molten volcanic ash droplets splat, accumulate and wet TBC substrates lack robust quantitative constraints. These complex processes are suspected to involve dynamic impact interactions (initial impact, rebounding or sticking, spreading and wetting, chemical reactions and interactions) of fine high-energy molten volcanic ash droplets with TBCs of jet engines.

Here, we employ an atmospheric plasma spray technology to generate high-energy molten volcanic ash droplets in the laboratory, as analogues of those present in operational jet engines. We observe splat formation, quantify their morphological evolution, and determine their adhesion capacity to conventional TBCs.

2. Experimental procedures

2.1 Preparation and characterization of the volcanic ash

The volcanic eruptive product used in this study is from the 2010 eruption of Eyjafjallajökull volcano, Iceland, which posed a major hazard to aviation safety [32]. Volcanic ash samples were prepared by crushing a volcanic bomb and subsequently milling the material in an agate mill (Fig. 2a). The bulk chemical composition of the volcanic ash sample was measured by X-ray fluorescence (Fig. 2b). The particle size distribution of the milled sample was obtained using the laser diffraction method (Fig. 2c). The D_{10}, D_{50} and D_{90} values constrain the smallest particle sizes, which contribute to define the coarsest 10%, 50% and 90% particle fractions of the cumulative volume distribution, respectively. Ash mineralogy was quantified using x-ray powder diffraction in a Panalytical X'Pert Pro MPD diffractometer fitted with an X'Celerator detector; the ash was mixed with 10 wt.% zincite (ZnO) and back-loaded into cavity holders as random powders. A copper X-ray tube was used with Ni filter to

select for Cu kα radiation and scans covered the 2θ range of 4-70°. Identification and quantification of the diffraction traces was performed manually using High Score Plus analysis software, by correlating peak height between the identified phases and the known fraction of zincite; once crystalline phase fractions were quantified, the rest was ascribed to the presence of amorphous material, primarily glass (Fig. 2d). The analysis indicates that the ash samples contain approximately 29% plagioclase, 6% clinopyroxene and 65% amorphous material.
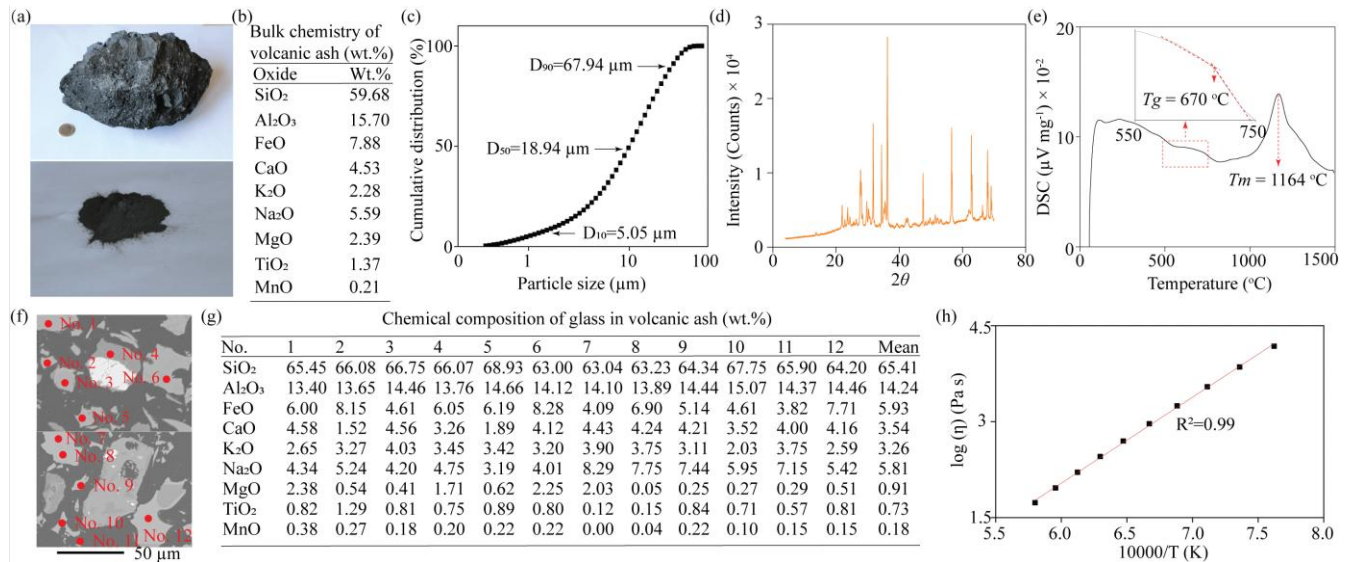

Bulk chemistry of volcanic ash (wt.%)

Oxide	Wt.%
SiO_2	59.68
Al_2O_3	15.70
FeO	7.88
CaO	4.53
K_2O	2.28
Na_2O	5.59
MgO	2.39
TiO_2	1.37
MnO	0.21

Chemical composition of glass in volcanic ash (wt.%)

No.	1	2	3	4	5	6	7	8	9	10	11	12	Mean
SiO_2	65.45	66.08	66.75	66.07	68.93	63.00	63.04	63.23	64.34	67.75	65.90	64.20	65.41
Al_2O_3	13.40	13.65	14.46	13.76	14.66	14.12	14.10	13.89	14.44	15.07	14.37	14.46	14.24
FeO	6.00	8.15	4.61	6.05	6.19	8.28	4.09	6.90	5.14	4.61	3.82	7.71	5.93
CaO	4.58	1.52	4.56	3.26	1.89	4.12	4.43	4.24	4.21	3.52	4.00	4.16	3.54
K_2O	2.65	3.27	4.03	3.45	3.42	3.20	3.90	3.75	3.11	2.03	3.75	2.59	3.26
Na_2O	4.34	5.24	4.20	4.75	3.19	4.01	8.29	7.75	7.44	5.95	7.15	5.42	5.81
MgO	2.38	0.54	0.41	1.71	0.62	2.25	2.03	0.05	0.25	0.27	0.29	0.51	0.91
TiO_2	0.82	1.29	0.81	0.75	0.89	0.80	0.12	0.15	0.84	0.71	0.57	0.81	0.73
MnO	0.38	0.27	0.18	0.20	0.22	0.22	0.00	0.04	0.22	0.10	0.15	0.15	0.18

Fig. 2. Physical and chemical characteristics of experimental volcanic ash. (**a**) Photographs of volcanic bomb sample collected from 2010 eruption of Eyjafjallajökull volcano, Iceland (left) and the experimental volcanic ash sample obtained by milling (right). (**b**) The bulk chemical composition constrained by the major oxides content (wt.%). (**c**) Cumulative volume distribution of the volcanic ash sample. (**d**) X-ray diffractogram of volcanic ash sample mixed with 10 wt.% zincite (ZnO). (**e**) DSC curve of the volcanic ash sample in oxidising atmospheric conditions under a heating rate of 10 °C min^{-1}; the data constrain the glass transition temperature, T_g (inset) and melting temperature T_m. (**f**) Backscattered-electron images of volcanic ash particles. The numbered red points indicate the position of chemical analyses with the electron-probe micro-analyser. (**g**) The chemical composition of glass in volcanic ash corresponding to the red points in Figure 2f. (**h**) Viscosity (η) of volcanic ash as a function of temperature (in Kelvin).

The melting behaviour of the sample was determined using a Netzsch 404 Pegasus differential scanning calorimeter (DSC) (Fig. 2e). In the DSC measurement, approximately 30 mg of sample was placed in a Pt crucible and heated at 10 °C min^{-1} from room temperature to 1490 °C under a constant air flow rate of 20 ml min^{-1}. The glass transition temperature, T_g, (the range of temperature over which the amorphous glass relaxes from a 'glassy' state to a liquid state with viscous response) was constrained at approximately 670 °C (shown in the inset in Fig. 2e). The second peak of the resultant DSC curve is interpreted to indicate crystal melting temperature, T_m, at *ca.* 1164 °C. The GRD model was used to

estimate T_g at 673 ºC (where viscosity is 10^{12} Pa s) based on the glass composition measured by electron-probe microanalysis (EPMA), consistent with our calorimetric T_g determination (Fig. 2e) [33]. Finally, the volcanic ash sample was re-melted at 1600 ºC and quenched in air; the quenched glass so obtained was crushed and then milled into powder. The powdered glass sample was then heated in a platinum crucible and the melt viscosity was measured at 1039-1451 ºC using a concentric cylinder viscometer [34]. The fitted viscosity data vs. temperature were used to constrain the rheological behaviour of in-flight molten volcanic ash droplets (the details in Ref. 34) (Fig. 2e).

2.2 **Characteristics of the substrates**
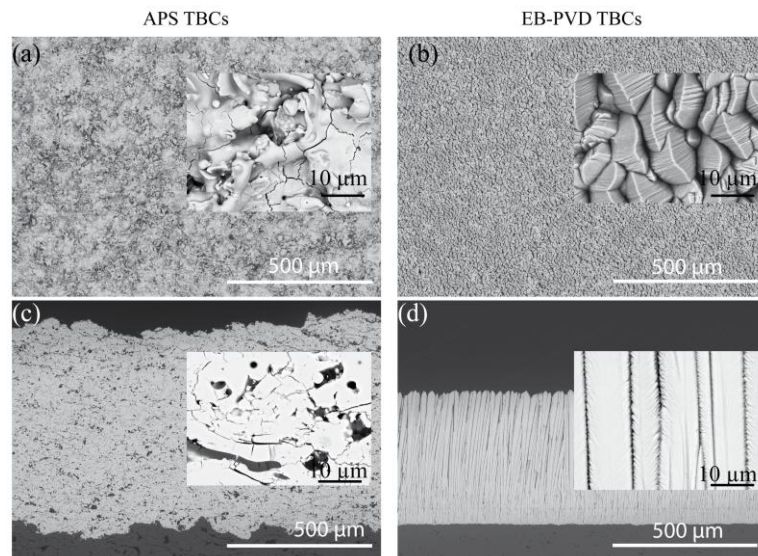
Fig. 3. Morphological characteristics of TBCs. (**a–b**) Top view SEM images of APS TBCs and EB-PVD TBCs used in these experiments. (**c–d**) Cross-section of SEM images of APS TBCs and EB-PVD TBCs. A higher magnification image of each coating is also shown in inset of figures with an enhanced contrast in order to emphasise microstructural features.

The thermal barrier coatings used in our experiments were fabricated at the German Aerospace Centre (DLR). Ceramic powder with a standard 7 wt.% Y_2O_3 stabilised ZrO_2 composition was deposited onto polycrystalline Al_2O_3 substrates by APS to produce 750 ± 20 µm thick coatings (i.e., APS TBCs), and the EB-PVD to form 450 ± 20 µm thick coatings (i.e., EB-PVD TBCs), respectively (Fig. 3). The surfaces of these two coatings were further carbon coated (low-vacuum coater EM ACE 200, Leica) to image the surface morphology via a JEOL JSM IT300LV scanning electron microscope (SEM) to observe the surface morphology (Figs. 3a-b). Next, the two coatings were mounted in epoxy resin discs to enable the analysis of their microstructures in cross-section (Figs. 3c-d).
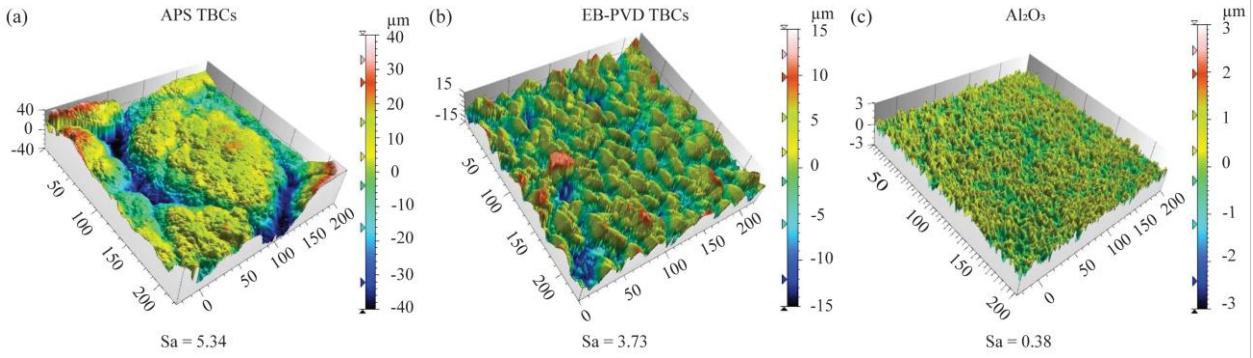
Fig. 4. Surface topographies of three types of substrates. (**a**) APS TBCs. (**b**) EB-PVD TBCs. (**c**) Al$_2$O$_3$ substrate.

The surface profiles of APS TBCs, EB-PVD TBCs, and alumina (Al$_2$O$_3$) substrates (used for a reference) were further quantitatively analysed using confocal laser scanning microscopy (LEXT, Olympus OLS 4100). Profile scanning was conducted (in the x, y direction of the surface) over an area of 200×200 μm^2 using a laser wavelength of 405 nm at a speed of 4 μm s^{-1} with a height (z) resolution of 0.05 μm. The surface profiles reconstructed were represented as 3-D digital images (Fig. 4). The surface roughness was evaluated using the roughness parameter, S_a, which represents the average of the absolute height values of $Z(x,y)$ in the measured area (A) and defined by $S_a = \frac{1}{A}\iint_A |Z(x,y)|dxdy$.

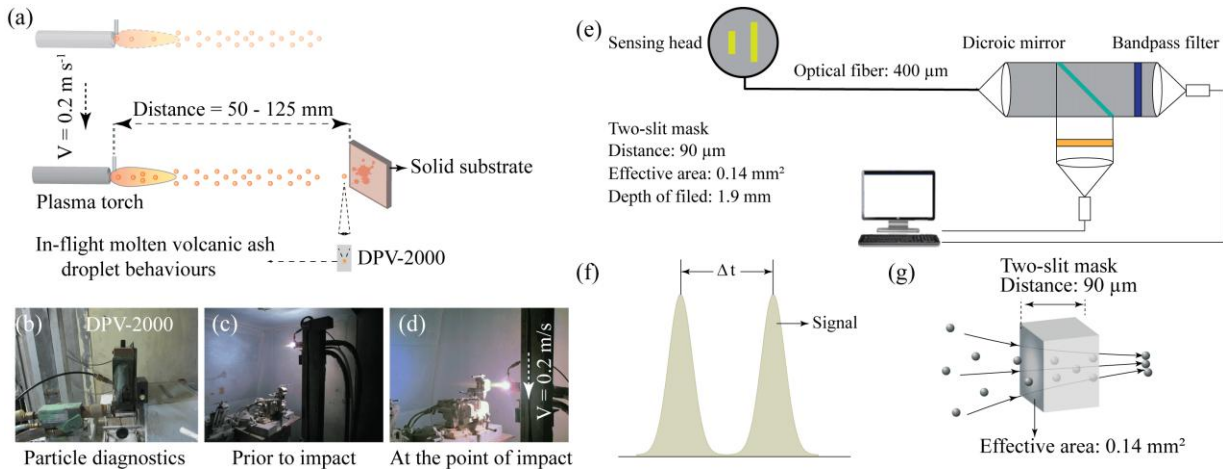## 2.3 Thermal plasma spraying process

Fig. 5. Experimental set-up. (**a**) Schematic illustration of the experimental setup used to investigate the impact of high-energy molten volcanic ash droplets onto solid substrates. (**b**) The particle diagnostics system (DPV-2000). (**c–d**) The specific experimental conditions (**c**) prior to impact and (**d**) at the point of impact. (**e**) Measurement setup for the particle diagnostic DPV-2000 system. (**f**) Signal (time versus intensity) generated from droplet passing in front of the dual slit for speed measurements. (**g**) Schematic diagram of definition of the droplet concentration.

Thermal plasma spraying was performed with a Oerlikon Metco 9 MB plasma spray at the Toyohashi University of Technology. During the plasma spraying process, volcanic ash particles were injected

8

into a plasma jet whereby they were rapidly imbued with high kinetic and thermal energy, and propelled towards the three substrates studied here (Fig. 5a) [35]. The spray parameters are listed in Supplementary Table 1. Here, three substrates have been employed; 1) traditional APS TBCs, 2) EB-PVD TBCs and 3) alumina (Al_2O_3) substrates exhibiting a relatively smooth surface (Fig. 4). The distances between the plasma torch and substrate were varied from 50 mm to 125 mm (in 25 mm increments) in order to alter systematically the in-flight properties (including droplet temperature, viscosity, velocity, diameter, and ash concentration) of these high-energy droplets prior to impact.

2.4 **Measurement of in-flight behaviour of molten volcanic ash droplets**

The characteristics of in-flight, molten, volcanic ash droplets (including droplet temperature, velocity, and diameter) prior to impact were measured by a DPV-2000 particle diagnostic system (Figs. 5b-d) [36]. For these purposes, the optoelectronic sensor head of the DPV-2000 was positioned near the solid substrate, and aligned perpendicular to the plasma jet, to characterise droplets properties immediately prior to their impact at distances of 50 mm to 125 mm from the torch as illustrated in Figure 5a. During a test, the sensor position from the torch could be automatically shifted to characterise maximum particle flux. A mask with two-slit in the sensing head was used to detect the light signals from a radiating particle as illustrated in Figure 5e. As a radiating droplet passes the two-slit mask of the optoelectronic sensor head, the droplet velocity (v) can be calculated in conjunction with the distance of the two silts d_{slit}, the arrival time of the two signals Δt, and the magnification factor of the lens f_{magn}, via $v = \frac{d_{slit}}{\Delta t} f_{magn}$ (Fig. 5f). Simultaneously, the surface temperature of a radiating droplet T was determined using a two-colour pyrometer by assuming this radiating particle was grey-body emitter with the same emissivity at two colour bands and then, calculating the ratio of the energy $E(\delta_i)$ radiated at two wavelength δ_i via $T_p = \omega(\frac{1}{\delta_1} - \frac{1}{\delta_2})/In(\frac{E(\delta_1)}{E(\delta_2)} \frac{\delta_1}{\delta_2}^5)$, where ω is a contant, 1.43×10^{-2} mK. The molten volcanic ash droplets are opaque at high temperature, therefore, the measured surface temperature may differ from that of the droplet core [37]. However, recent experimental work has

indicated that the temperature difference between the surface and centre of a droplet is insignificantly small [38]. Hence, we assume that the droplet temperature is homogeneous and that the droplets are fully molten at the points of measurement and impact with the solid substrate. The droplet diameter d, was estimated based on the assumption that the droplets are spherical; the diameter is obtained from the radiation energy emitted at a single wavelength using $d_p = \sqrt{E(\delta_i)/f_{diam}}$, where f_{diam} was a calibration factor [36]. Finally, the in-flight droplet concentration is defined as the total mass of molten volcanic ash droplets per unit volume. The ash concentration C was calculated using the mass of high-energy droplet passing through the measuring volume of the sensor head per second, via $C = \frac{\sum_{i=1}^{N} v_i \rho}{A(v_i t_i)_{max}}$, where N is the total number of volcanic ash droplets passing through in a unit area, A=0.14 mm^2, v_i and t_i are the volume and time of an in-flight molten droplet i, ρ is the droplet density, 2029 kg m^{-3}, and the subscript 'max' represents the maximum number of droplets present in the measurement space (Fig. 5g).

2.5 Estimation of droplet concentration safety threshold for 'safe-to-fly' in a realistic jet engine condition

Based on the assessment of aviation safety by ICAO, volcanic ash clouds with an ash concentrations greater than 2-4 mg m^{-3} are considered hazardous for commercial airlines [39,40]. However, considering that the operating pressure in a jet engine is higher than atmosphere pressure, the ash concentration in the hot section of jet engines increases as the air density increases; thus, the ash concentration threshold of 2-4 mg m^{-3} in volcanic ash clouds at atmospheric pressure may not necessarily be applicable to adequately delimit this hazard.

Ash concentration in jet engines is determined by air density, controlled by pressure and temperature [41]. Air entering a jet engine, is first compressed by the fan. Then it passes through the low-pressure and subsequently high-pressure compressors, before flowing through the constant-pressure combustion, nozzle guide vanes and high-pressure turbine blades. The highest pressure in the jet engine is observed

at the compressor exhaust. Thus the ash concentration of this section can be regarded as the maximum value encountered in the entire jet engine. and is used here as a safety threshold of droplet concentration for the entire jet engine. We can estimate the ash concentration in a jet engine using the thermodynamic ideal cycle analyses in a jet engine [42]. The ash concentration ratio under isentropic compression is proportional to the pressure ratio, which is denoted as $\frac{c_0}{c_1} = (\frac{P_0}{P_1})^{\frac{1}{\kappa}}$, where P is the air pressure (Pa), κ is the ratio of heat capacity (κ =1.4 for air [43]), and the subscripts 0 and 1 denote the inlet and exit pressure of the compressor, respectively. In an ideal open jet engine, the compressor inlet pressure is equal to the ambient pressure. Atmospheric air parameters (pressure, temperature and density) are changing with altitude above sea level, which affects the performance of aircraft engines [44]. Here, international standard atmosphere is used as the ambient condition, in which it is assumed that at sea level the air pressure is 101 kPa and temperature is 288.15 K. The compressor exhaust section pressure is defined as the final condition, which is around 1110 kPa N [45]. Therefore, the specific value of the hazard threshold of droplet concentrations in jet engine is 27.16 mg m^{-3}, based on the 4 mg m^{-3} of ash concentration in the volcanic ash cloud.

2.6 **Substrate temperature measurement in the thermal spray process**

To determine the influence of radiative heating of the substrate surface by the thermal plasma gun, we employed a Type-S thermocouple to monitor the change of temperature during a single spraying event. To reduce the effect of a lag in heat transfer through the alumina protective tube, we deployed the thermocouple without the protective alumina sheath and located it at the same position as the substrate. The heating profile experienced by the Type-S thermocouple at each distance condition was measured, and the evolution of surface temperature of APS TBCs, EB-PVD TBCs, and Al_2O_3 substrate was estimated using Fourier's law in a one dimensional differential form for diffusive heat transfer: $q = -k\, dT/dx$, where q is the local heat flux density (W·m^{-2}), k is thermal conductivity ($k_{APS\ TBC}$ = 1.0 W m^{-1} K^{-1}, $k_{EB\text{-}PVE\ TBC}$ = 1.7 W m^{-1} K^{-1} and k_{Al2O3} = 35 W m^{-1} K^{-1}) [46,47], T is the local temperature (°C), and t is time (s). The maximum temperature value in each heating profile between the torch and

11

the substrate is regarded as the substrate surface temperature during impact of droplets fired from different distances.

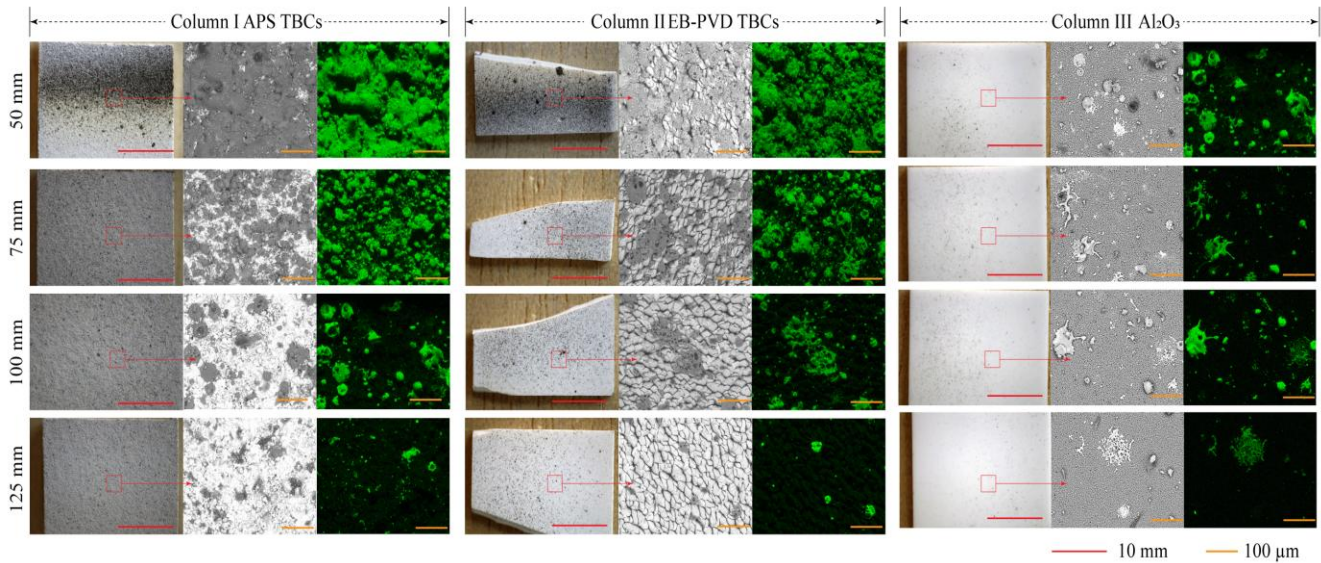## 2.7 Single splats formation on TBCs and Al$_2$O$_3$ substrates in the initial impact experiment

Fig. 6. Initial impact behaviour of molten volcanic ash droplets on APS TBCs (column I), EB-PVD TBCs (column II), and Al$_2$O$_3$ (column III) substrates. The left, middle, and right sub-columns in each column display the photographs, SEM images, and Si elemental mappings corresponding to the SEM images of various substrates impacted by the molten volcanic ash droplets with torch distances from 50 mm to 125 mm, respectively. Note that the irregularly shaped EB-PVD TBCs were caused by handling damage before the experiment took place.

In order to investigate the initial droplet impact behaviour as well as to remove complexities arising from splat overlaps during stable spraying conditions, we first performed a simple, short-lived spray test onto each one of the solid substrates; yet to prevent splat overlaps from the jet. In the initial impact experiment (utilising a single spray treatment), the perpendicularly mounted thermal spray gun sprayed the three kinds of substrates (APS TBCs, EB-PVD TBCs, and Al$_2$O$_3$ substrates) with droplets and was migrated over the substrate at a speed up to 0.2 m s^{-1} at torch distances of between 50 mm and 125 mm during the brief spray test (Fig. 5a). The impacted surface of all substrates was examined both optically (with a Canon camera) and microscopically (by SEM) (Fig. 6). The silicate ash droplets adhered onto the surfaces of the three substrates were characterised using energy dispersive spectroscopy (EDS).

12

Elemental mapping of silicon was performed with spatial resolution of 1 μm per pixel to obtain an accurate picture of the ash distribution.

2.8 Morphology identification of isolated splats deposited on TBCs and Al_2O_3 substrates
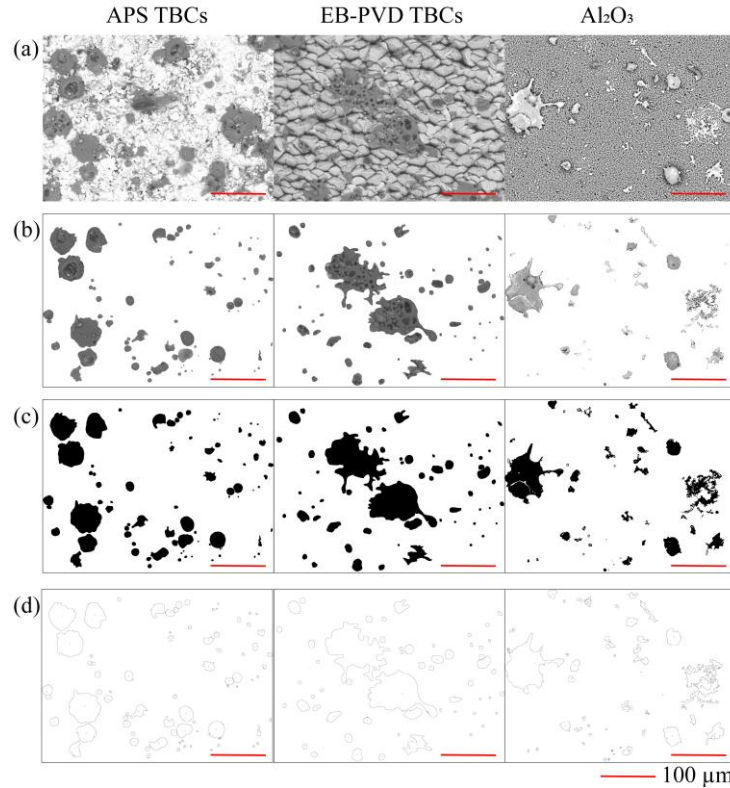

Fig. 7. Identification morphology process of initial isolated splats adhered on the various substrates. (**a**) Original SEM images of APS TBCs, EB-PVD TBCs, and Al_2O_3 substrate impacted by molten volcanic ash droplets from experiments conducted at a torch distance of 100 mm. The corresponding grayscale morphologies (**b**), binary morphologies (**c**), and labelled boundaries (**d**) of splats observed on each substrates are also displayed.

SEM images of both APS TBCs and EB-PVD TBCs from experiments conducted at a torch distance of 100 mm as well as Al_2O_3 substrate from experiments conducted at torch distances of 50 mm to 125 mm, respectively, were analysed after the initial impact (i.e., single spray). The select tool in Adobe Photoshop element 15 was used to automatically identify the edge of manually selected splat. Each splat was selected from the original SEM grayscale images where each splat could be observed at high magnification (Fig. 7a and Fig. 8a). Grayscale images of each splat marked in Fig. 7b and Fig. 8b were converted to binary images (i.e.., black and white) with the threshold method (threshold value = 235 and scale = 6.06 pixel/μm) and finally the edge of each splat was detected and labelled by Image J software (Figs. 7c-d and Figs. 8c-d) [49]. The geometric parameters of the morphology of each splat

(including splat area, perimeter and circularity) were obtained and the total number of splats observed was counted using the Image J software. The statistical analysis of geometric parameters of the morphology of each splat on APS TBCs, EB-PVD TBCs and Al_2O_3 substrate are presented in Supplementary Tables 2 and 3.
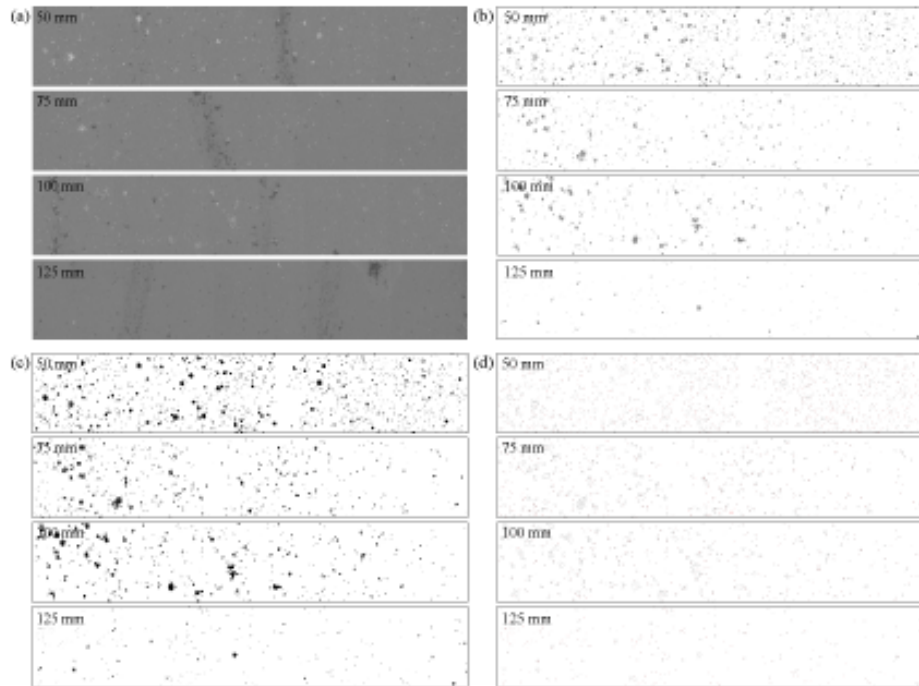

Fig. 8. Morphological identification images of isolated splats adhered on the Al_2O_3 substrates from experiments conducted at the different torch distances. (**a**) Original SEM images of Al_2O_3 substrates initially impacted by molten volcanic ash droplets from experiments conducted at torch distances of 50 mm to 125 mm. The corresponding grayscale morphologies (**b**), binary morphologies (**c**), and labelled boundaries (**d**) of splats observed in each substrates are also displayed.

2.11 Calculation of adhesion rate of the in-flight molten volcanic ash droplets in the deposition experiment

To determine the adhesion rate of molten volcanic ash droplets on each substrate, we weighed the substrate before and after the spray test at various spraying distances. However, owing to the insignificant amount of ash adhered to the substrate, we did not detect any weight differences between the original versus the sprayed substrate, even when sprayed from a distance of 50 mm. Therefore, in order to resolve the adhesion rate, we repeated the spray test ten times to accumulate sufficient ash on each substrate (see Supplementary Table 4). Note that the absolute weight increase depends on the effective substrate area onto which droplets adhere, which varies for each conditions and substrates. To

14

eliminate the interference from the difference of original effective deposited area of each substrate, we normalized the original weight by defining adhesion rate, ε, (namely, mass accumulation rate) as a relative change in weight, $\varepsilon = \frac{w_1 - w_0}{w_0} \times 100\%$, where w_0 and w_1 are the weight of substrate before and after the deposition experiment.
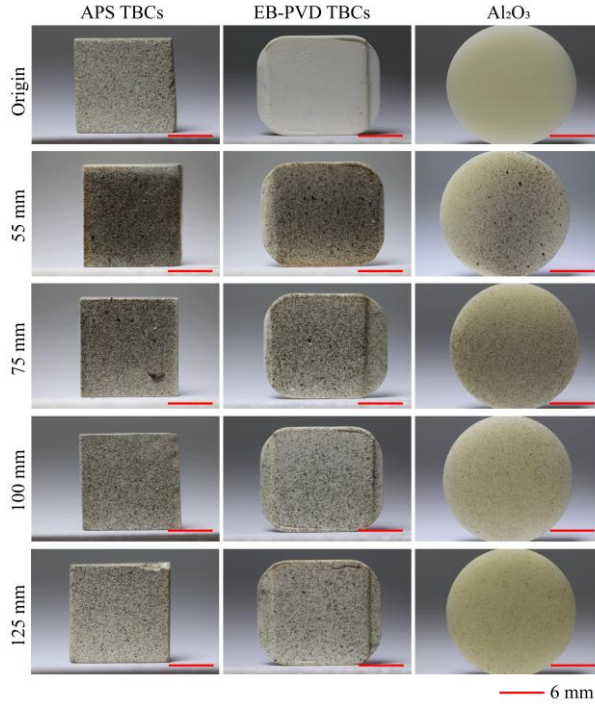

Fig. 9. Photographs of the original and post-deposition APS TBCs, EB-PVD TBCs, and Al_2O_3 substrates from deposition experiments conducted at torch distances from 50 mm to 125 mm, respectively.

3. Results and discussions

3.1 The characteristics of in-flight molten volcanic ash droplets

The characteristics of in-flight molten volcanic ash droplets were measured by DPV-2000 and subsequently analysed statistically. The total number of droplets monitored at each spray distance condition was between 3000 and 5000 droplets over 14–55 s. The properties of the in-flight molten droplets at each distance condition were measured and analysed, and the distribution of the related parameters are presented as a histogram in Fig. 10. These parameters contain experimentally measured parameters (involving droplet temperature, velocity, diameter). These measured parameters distributions are approximated by Gaussian normal distribution functions. To reduce the disturbance from outliers in a dataset, the 5% trimmed distribution (when the lowest 5% and the highest 5% of

15

values are discarded) were applied to the Gaussian correlation. The associated statistical analysis corresponding to the characteristics of in-flight molten volcanic ash droplets prior to impact are provided in Supplementary Table 5.
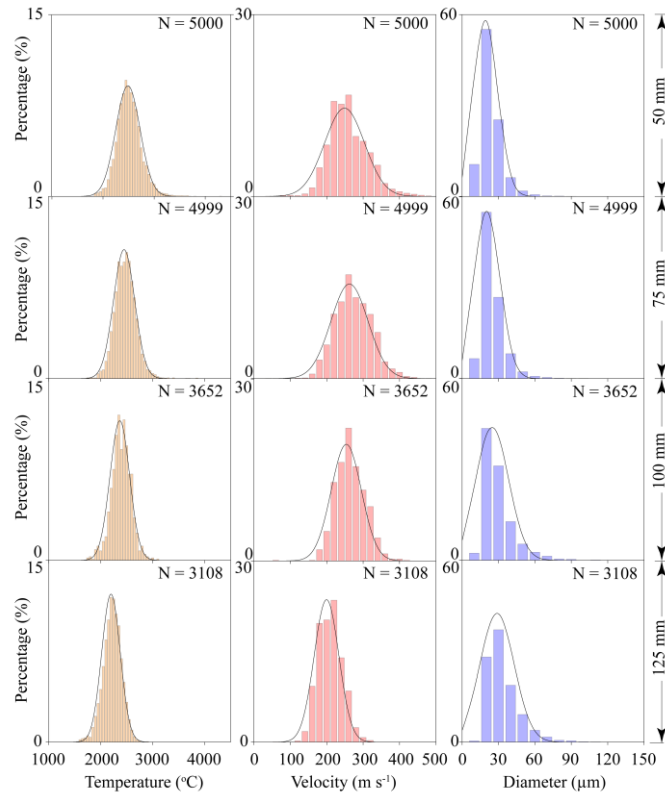

Fig. 10. Histograms of the characteristics of in-flight molten volcanic ash droplets under various distance conditions. Droplet temperature distributions (column I), droplet velocity distributions (column II), droplet size distributions (column III) of in-flight molten volcanic ash droplets measured by DPV-2000 at the distances to the torch of thermal spray gun between 50 mm and 125 mm. The black lines represent the best-fitting Gaussian line profiles. *N* indicates sample size (i.e., the number of volcanic ash particles monitored at each distance condition).

At each spraying distance, high-energy molten volcanic ash droplets were successfully generated. The average droplet temperatures decrease from 2550 ºC to 2200 ºC; and the ash concentration decreases from 60 mg m^{-3} to 21 mg m^{-3} , with increasing spray distance. The droplets have near-constant sizes of 20 μm to 27 μm and experience subsonic velocities of 199 m s^{-1} to 262 m s^{-1}) (Figs. 11a-c). These average velocities and droplet sizes are comparable to those anticipated under the conditions of operation in current jet engines. The average droplet temperatures and the droplet concentrations constrained during the tests exceed the operating temperatures of jet engines (1200-1500 ºC) and the recommended maximum concentrations of ash in jet engines (i.e., 27 mg m^{-3}; Fig. 11d).
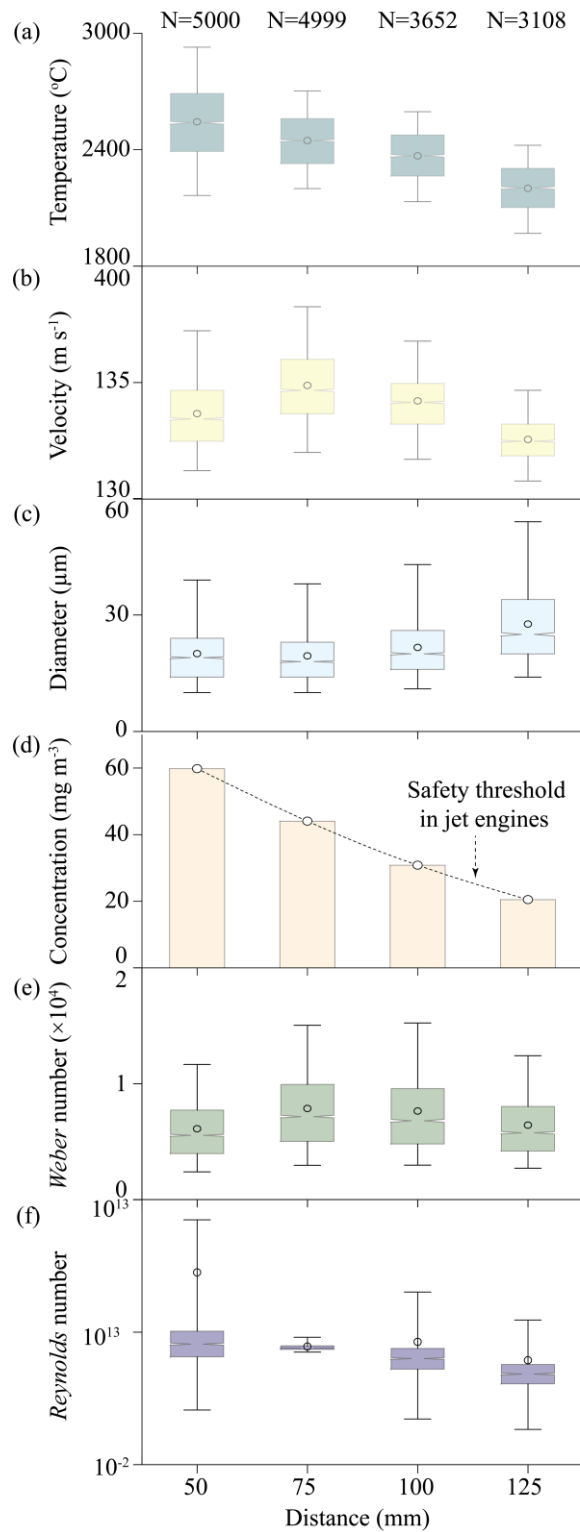
16

Fig. 11. Experimentally measured parameters involving (**a**) droplet temperature, (**b**) velocity, (**c**) diameter and calculated parameters involving (**d**) droplet concentration, (**e**) *Weber* number and (**f**) *Reynolds* number) of in-flight molten volcanic ash droplets prior to impact as a function of the distance between the plasma torch and the solid. Box-and-whisker plots represent (hollow circles), 25th–75th percentiles (boxes) and 5th–95th percentiles confidence intervals (whiskers) (N = number of data points).

In order to generalise the characteristics of an individual in-flight high-energy molten volcanic ash

droplet before impact onto the substrate, we employ the Weber number (*We*) and Reynolds number

17

(*Re*) (Figs. 11e-f) [50,51]. The *We* number is the ratio between inertial and the surface tension forces, whereas *Re* number is the ratio between inertial and viscous forces. The *We* number is not only a ratio of time scales but also a measure of the energy of the droplet. The *Re* number quantifies the relative importance of inertial forces and viscous forces. The *We* and *Re* numbers are defined as $We = \rho \cdot v_p^2 \cdot d_p/\sigma$ and $Re = \rho \cdot v_p \cdot d_p/\mu$, respectively, where v_p is the velocity of an in-flight particle (m s^{-1}), d_p is its diameter (m), ρ is its density (kg m^{-3}), σ is its surface tension (N m^{-1}), and μ is its viscosity (Pa s). These two dimensionless constraints provide a greater capability (than single parameters; e.g., velocity or temperature) to reflect in-flight characteristics and physical properties of molten volcanic ash droplets. Surface tension of silicate melts only slightly varies over a wide range of temperatures and is defined as a constant number of 0.36 N m^{-1} [34]. The viscosity of a volcanic ash melt decreases exponentially with increasing temperature [52], leading to a wide distribution of *Re* at each condition.

3.2 The thermal history of various substrates in the thermal spray process
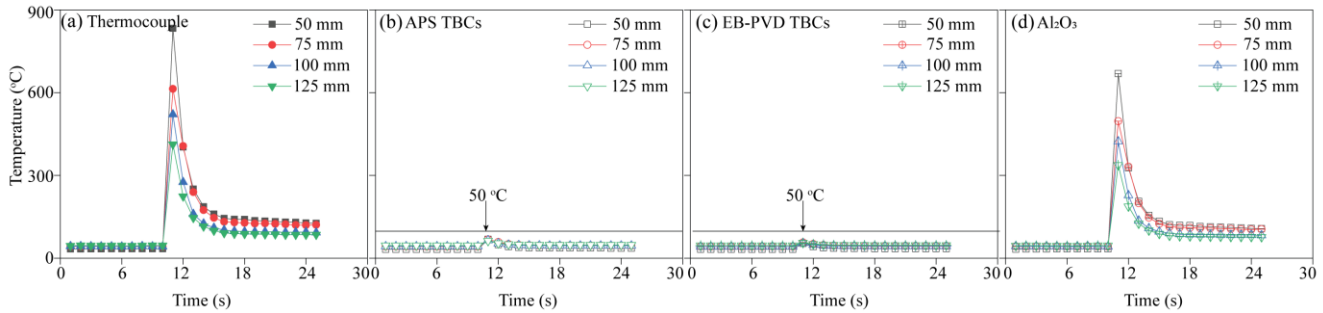

Fig. 12. Surface temperature evolution of substrates in the initial droplet impact process. The temperature variation of (**a**) Type-S thermocouple measured, (**b**) APS TBCs, (**c**) EB-PVD TBCs and (**d**) Al$_2$O$_3$ substrates as a function of time at torch distances from 50 mm to 125 mm.

The surface temperature of each substrate (i.e., APS TBC, EB-PVD TBC, and Al$_2$O$_3$) was monitored by a thermocouple (Fig. 12) and found to be far lower than the characteristic temperatures of melting of crystalline phases in these hot droplets (~1164 ºC, as estimated via differential scanning calorimetry). The maximum temperature increase in the substrate during the impact experiment was 50 ºC for both APS TBC and EB-PVD TBC, and 600 ºC for the Al$_2$O$_3$ substrate. This low substrate temperature

promotes rapid cooling of droplets upon impact. We therefore consider our experiments to take place in a simplified scenario whereby a hot droplet collides with a cooler substrate.

3.3 Splat formation by in-flight molten volcanic ash droplets

The molten droplet impact process is highly complex [53,54]. Generally, when a single high-energy molten droplet impacts a cold substrate, it first deforms, and then spreads and/or splashes. The droplet consequently solidifies as a splat of variable morphology [55,56]. Splat morphology, in turn, plays a key role in controlling the mechanical properties of volcanic ash deposits on TBCs, and dictates their capacity to adhere to the surface. Hence, constraining the variables which control both splat formation and evolution is essential for the understanding of volcanic ash deposition in jet engines.
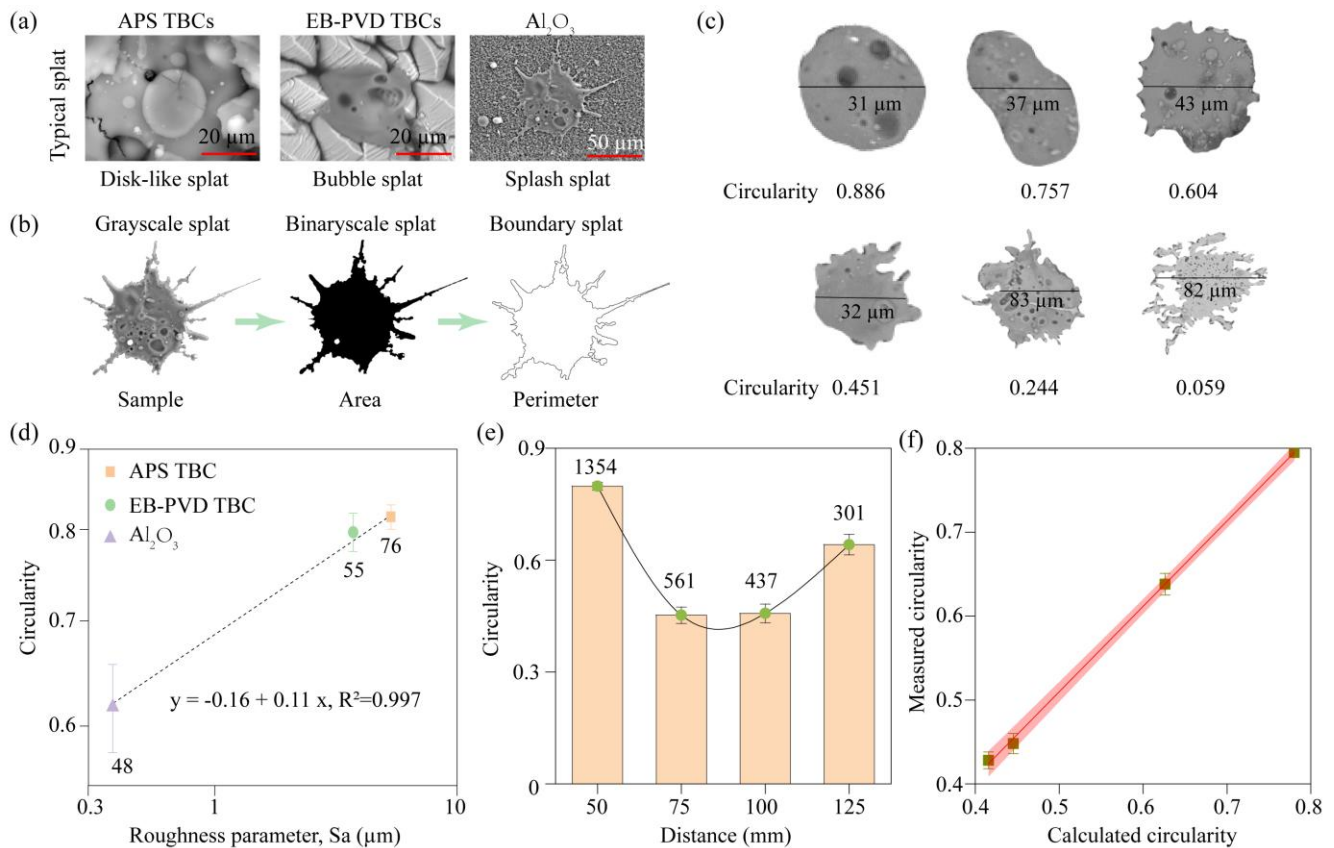

Fig. 13. The morphology of molten volcanic ash splats on the various substrates. (**a**) SEM images of typical splat micrographs on APS TBCs, EB-PVD TBCs and Al_2O_3 substrates impacted by molten volcanic ash droplets at a torch distance of 100 mm. (**b**) Splat image analysis and morphology characterization. (**c**) Changes in the morphology of selected splats on Al_2O_3 substrates with decreasing splat circularity. (**d**) The circularity of splats on each substrate at a torch distance of 100 mm identified from Fig. 7 as a function of substrate roughness, S_a. The dashed line is the linear best fit. The number of circularity measurements for splats on each substrate are indicated numerically below each data point. (**e**) Changes in the circularity of splats on Al_2O_3 substrates with increasing torch distance, with the sample size indicated numerically above each column. **f**, Comparison between measured and calculated circularities of splats on the Al_2O_3 substrates across all torch distances. The red-shaded areas correspond to 95% confidence intervals.

19

To a first approximation, the morphologies of single splats shown in Figure 13a can be defined by their circularities [57], which is a quantification of the relationship between the area and the perimeter of the splat; circularity $= 4\pi Area/perimeter^2$ (Fig. 13b). A circle has therefore a circularity of 1. The smaller the value, the less circular the splat is (Fig. 13c).

Splat morphology is controlled by a combination of factors arising from 1) the surface properties of substrates, and 2) the characteristics of in-flight droplets at the point of impact. For a given distance (and thereby thermo-physical state of in-flight droplets), the surface roughness has been identified as a principal topographic parameter determining splat formation. Within the range of torch distances ($50 \leq$ 125 mm) tested here, we have chosen the spray tests performed at a distance of 100 mm from the substrate for in-depth analysis, because the resultant well-dispersed splat distributions allow individual splat analysis (Fig. 7). [Note that in experiments at smaller torch-substrate distances, significant overlapping of splats obscures the observation of single splats, whilst at greater distance, many splats are so excessively dispersed as not to be fully amenable for quantitative analysis (Fig. 6). We observe a proportionality between the mean splat circularity and the substrate roughness parameter, S_a (Fig. 13d), as observed in previous studies [58]; as the substrate roughness decreases, splat morphology becomes increasingly variable and unstable, resulting in radial jetting and break-up. Thus, droplet impacts on smooth surfaces (e.g., Al_2O_3) produce a greater abundance of 'splash'-shaped splats, while rougher surfaces (e.g., APS TBCs) tend to exhibit 'disc' shapes (Fig. 13a). These discs are indicative of a tendency for a smoother surface yield higher flow speeds of the leading edge of the splat over substrate asperities, which may in turn promote the formation of a 'splash' morphology.

The thermo-physical properties of in-flight molten droplets are an additional control on the splat morphology of cold substrates. Their influence is felt through the transfer of kinetic and thermal energy of the droplet before impact, through viscous energy dissipation during impact (*i.e.*, work done in deforming the droplet against viscosity), and surface energy after impact. To elucidate the influence of in-flight molten droplet properties on splat morphology, we have analysed the evolution of the splat

20

circularity on the Al$_2$O$_3$ substrates (where the volcanic ash splat is more uniformly distributed compared to APS and EB-PVD TBCs) with increasing torch distance from 50 mm to 125 mm (Fig. 13e). The characteristics of in-flight molten droplets before impact onto the substrate (including temperature, velocity, and droplet diameter), are described by two dimensionless parameters: the Weber number (*We*) and Reynolds number (*Re*) [59]. Multiple linear regressions were used to correlate *We* and *Re* numbers with circularity, and the empirical parameters obtained from this analysis cast the following relationship, circularity $= 10^{7.79}We^{-2.1}Re^{0.0092}$ (Supplementary Table 6). Comparison of the visual observations of splat morphology with those predicted by the We and Re relationship demonstrate a good fit of the regression with a 95% confidence interval shaded in red (Fig. 13f), indicating this model can be employed to describe the splat formation morphology under the differing in-flight states of each droplet.

3.4 Adhesion rate of in-flight molten volcanic ash droplets on various substrates
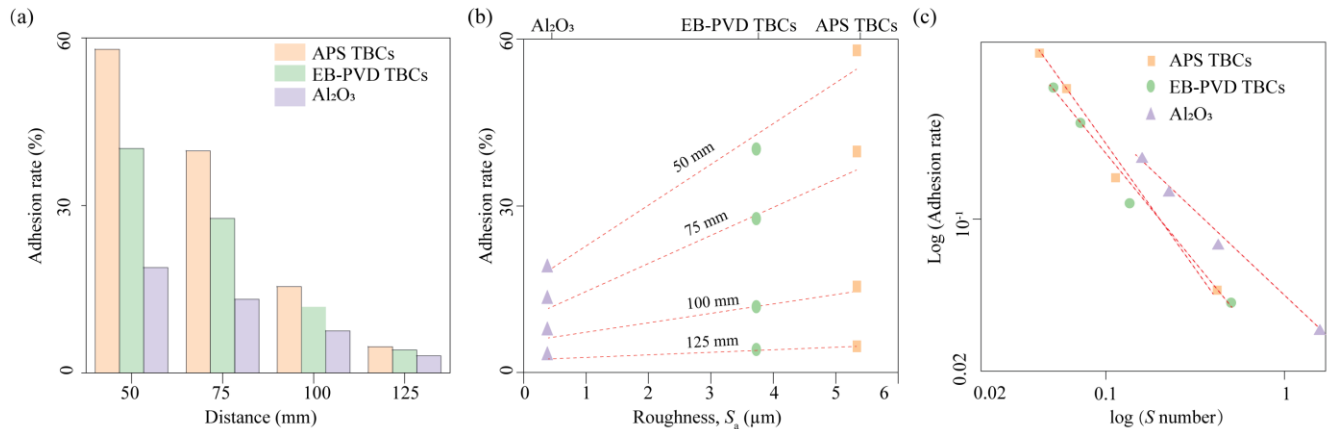
Fig. 14. Deposition characteristics of in-flight molten volcanic ash droplets on the various substrates. (**a**) Evolution of adhesion rate of molten volcanic ash droplets with increasing torch distance and varying substrates. (**b**) Adhesion rate of molten volcanic ash droplets as a function of the substrate roughness, S_a, for the three substrates (APS TBCs, EB-PVD TBCs, and Al$_2$O$_3$ substrate) at four torch distances. (**c**) Adhesion rate of molten volcanic ash droplets onto APS TBCs, EB-PVD TBCs, and Al$_2$O$_3$ substrate as a function of the dimensionless number, S, plotted on a logarithmic axis. The dotted red lines in Figs. 14 **b** and **c** show the best-fit linear regression; the parameters corresponding to these regressions are displayed in Supplementary Tables 7 and 8.

After performing the initial single-spray tests, the noticeable variability of deposition behaviour of in-flight molten droplets as functions of substrate and distance is a clear indication that not all high-energy droplets adhere to the substrates; rather, some rebound from the substrate surface (Fig. 6). To quantify

the probability that high-energy molten volcanic ash droplets will adhere to the substrate, we performed deposition experiments and determined the adhesion rate (ε) of droplets (namely, mass accumulation rate of splats) on the substrates over time, and in relation to substrate type and in-flight molten droplets condition. Distinct depositional behaviours on the three substrates have been observed in experiments at constant torch distance (Fig. 9 and Fig. 14a), indicating the adhesion rate of droplets onto substrates is dictated equally by properties of substrates and in-flight hot droplet characteristics.

Firstly, there is a linear correlation between the adhesion rate and substrate roughness (S_a) at a given torch-substrate distance, which indicates that roughness of substrate is most probably key parameter on controlling the adhesion rate of molten volcanic ash droplets (Fig. 14b). In addition, for any given torch-substrate distances, the adhesion rates on the roughest APS always exceed that of rough EB-PVD TBCs and the smoothest Al_2O_3 substrate, which is consistent with the idea that development of smooth substrate surface is essential to mitigate the likelihood of molten volcanic ash droplet adhesion to hot components within jet engines.

Secondly, adhesion rate also varies with torch distance, implying that droplet properties (e.g., droplet temperature, velocity, diameter, and concentration) also govern the adhesion efficiency of these droplets onto a given substrate, where droplet temperature, viscosity and concentration have the high contribution to adhesion efficiency (See Supplementary Figure 1). To account for all thermo-physical properties of in-flight droplets and quantitatively constrain their influence, here, we develop a new dimensionless number, termed the S number , $S = \frac{\sqrt{We \cdot d_p / s_a} \cdot C \cdot v}{Re \cdot C_S \cdot Ma}$, where C is the droplet concentration, mg m^{-3}, d_p is the droplet diameter, μm, S_a is the substrate roughness, μm, C_S is the estimated safety threshold of droplet concentration in jet engines, 27.4 mg m^{-3}, v is the mean of droplet velocity, and Ma is the Mach number. This dimensionless parameter of in-flight volcanic ash droplet properties not only provides a good correlation with the adhesion rate on each substrate but also links droplet properties and substrate properties, causing the datasets for APS and EB-PVD TBCs to collapse onto a

single curve, with only minor departures (Fig. 14c). Hence, we propose the use of *So* as a parameter to simplify the description of the thermo-physical properties of in-flight molten volcanic ash droplets in its interaction upon impact with various substrates.

4. Conclusions

The systematic description of the characteristics of in-flight high-energy molten volcanic ash particles in a combustion environment and their impact on various substrates (APS TBCs, EB-PVD TBCs, and Al_2O_3 substrates) support the following conclusions drawn from this work:

(a) The surface roughness of a substrate plays a key role in controlling the morphology of splats resulting from the impact of molten volcanic ash droplets onto TBCs. In particular, smooth surfaces promote the formation of a 'splash' morphology with radial jetting and break-up, whereas rougher surfaces (e.g., APS TBCs) tend to promote the development of circular, 'disc' shape splats. This is due to higher flow speeds of the leading edge of a splat over smoother substrates; whereas asperities on rough surfaces restrict flow.

(b) TBCs surface properties and in-flight characteristics of high-energy molten volcanic ash droplets are the dominant controls on the splat accumulation. Hotter droplets with lower viscosity, striking a rougher substrate with large velocity components normal to the surface of substrate, are more likely to adhere to TBCs. A new dimensionless parameter S_o was developed to quantitatively constraint the influence of in-flight volcanic ash droplet properties and substrate roughness on adhesion rate.

To accelerate the development of reliable mitigation protocols for volcanic ash–jet engine interaction, we propose that the well characterised volcanic ash samples described here should be employed in future engine operation testing to assess the relative propensities of natural ash particles to adhere to, and interact with, jet engine coatings. Our results provide a basis for the improvement of current and next-generation APS and EB-PVD TBCs to improve their resistance to volcanic ash and other silicate

23

deposits (sand, dust, fly ash), particularly as higher and higher temperature turbine operating conditions become increasingly dominant in both aircraft propulsion and land-based electricity generation.

Acknowledgements

References

1. A. J. Prata, I. J. Barton, R. W. Johnson, K. Kamo, J. Kingwell. Hazard from volcanic ash. *Nature* 354 (1991) 25. DOI:10.1038/354025a0.

2. K. Sanderson. Questions fly over ash-cloud models. *Nature* 464 (2010) 1253. DOI:10.1038/4641253a.

3. T. J. Casadevall. Volcanic hazards and aviation safety-lessons of the past decade. *FAA Aviation Safety J.* 2 (1992) 9–17.

4. W. Song, Y. Lavallée, K. U. Hess, U. Kueppers, C. Cimarelli, D. B. Dingwell. Volcanic ash melting under conditions relevant to ash turbine interactions. *Nat. Commun.* 7 (2016) 10795. DOI:10.1038/ncomms10795.

5. P. Webley, L, Mastin. Improved prediction and tracking of volcanic ash clouds. *J. Volcanology Geotherm. Res.* 186 (2009) 1–9. DOI:10.1016/j.jvolgeores.2008.10.022.

6. M. Guffanti, D. J. Schneider, K. L. Wallace, T. Hall, D. R. Bensimon, L. J. Salinas. Aviation response to a widely dispersed volcanic ash and gas cloud from the August 2008 eruption of Kasatochi, *Alaska*, USA. *J. Geophys. Res. Atmos.* 115 (2010) D00L19. DOI:10.1029/2010JD013868.

7. R. Gertisser. Eyjafjallajökull volcano causes widespread disruption to European air traffic. *Geol. Today.* 26 (2010) 94–95. DOI: 10.1111/j.1365-2451.2010.00757.x.

8. L. Jiang, Y. Han, P. Patnaik. Characteristics of volcanic ash in a gas turbine combustor and nozzle guide vanes. ASME. *J. Eng. Gas. Turbine Power* 140 (2018) 071502. DOI:10.1115/1.4038523.

9. W. Song, K. U. Hess, D. E. Damby, F. B. Wadsworth, Y. Lavallée, C. Cimarelli, D. B. Dingwell. Fusion characteristics of volcanic ash relevant to aviation hazards. *Geophys. Res. Lett.* 41 (2014) 2326–2333. doi:10.1002/2013GL059182.

10. A. D. Gledhill, K. M. Reddy, J. M. Drexler, Shinoda, K., Sampath, S. & Padture, N. P. Mitigation of damage from molten fly ash to air-plasma-sprayed thermal barrier coatings. *Mater. Sci. Eng. A* 528 (2011) *7214*–7221. DOI: 10.1016/j.msea.2011.06.041.

11. F. R. Martínez, A. A. R. Martínez, M. T. Velazquez, P. Q. Diez, G. T. Eslava, J. A. Francis. Evaluation of the gas turbine inlet temperature with relation to the excess air. *Energy Power Eng.* 3 (2011) 517–524. DOI:10.4236/epe.2011.34063.

12. S. Roux, M. Cazalens, T. Poinsot. Outlet-boundary-condition influence for large eddy simulation of combustion instabilities in gas turbines. *J. Propul. Power* 24 (2008) 541–546. DOI:10.2514/1.33739.

13. S. Chandra, P. Fauchais. Formation of solid splats during thermal spray deposition. *J. Therm. Spray Technol.* 18 (2009) 148–180. DOI: 10.1007/s11666-009-9294-5.

14. W. Ai, N. Murray, T. H. Fletcher, S. Harding, P. B. Jeffrey. Effect of hole spacing on deposition of fine coal fly ash near film cooling holes. *J. Turbomach.* 134 (2011) 041021. DOI: 10.1115/1.4003717.

15. N. P. Padture, M. Gell, E. H. Jordan Thermal barrier coatings for gas-turbine engine applications. *Science* 296 (2002) 280−284. DOI:10.1126/science.1068609.

16. N. P. Padture. Advanced structural ceramics in aerospace propulsion. *Nat. Mater.* 15 (2016) 804–809. DOI:10.1038/nmat4687.

17. D. R. Clarke, C. G. Levi. Materials design for the next generation thermal barrier coatings. *Annu. Rev. Mater. Res.* 33 (2003) 383−417. DOI: 10.1146/annurev.matsci.33.011403.113718.

18. C. G. Levi. Emerging materials and processes for thermal barrier systems. *Curr. Opin. Solid State Mater. Sci.* 8 (2004) 77−91. DOI:10.1016/j.cossms.2004.03.009.

19. S. Sampath, U. Schulz, M. O. Jarligo, S. Kuroda. Processing science of advanced thermal-barrier systems. *MRS Bull.* 37 (2012) 903–910. DOI: 10.1557/mrs.2012.233.

25

20. R. Sivakumar, B. L. Mordike. High Temperature coatings for gas turbine blades: A Review. *Surf*. *Coat*. *Technol*. 37 (1989) 139–160. DOi:10.1016/0257-8972(89)90099-6.

21. H. Zhao, C. G. Levi, H. N. G. Wadley. Molten silicate interactions with thermal barrier coatings. *Surf*. *Coat*. *Techol*. 251 (2014) 74–86. DOI:10.1016/j.surfcoat.2014.04.007.

22. B. Zhang, W. Song, H. Guo. Wetting, infiltration and interaction behaviour of CMAS towards columnar YSZ coatings deposited by plasma spray physical vapor. *J*. *Eur*. *Ceram*. *Soc*. 38 (2018) 3564–3572. DOI:10.1016/j.jeurceramsoc.2018.04.013.

23. T. J. Casadevall. The 1989–1990 eruption of redoubt volcano, Alaska: impacts on aircraft operations. *J*. *Volcanol*. *Geotherm*. *Res*. 62 (1994) 301–316. DOI: 10.1016/0377-0273(94)90038-8

24. M. G. Dunn. Operation of gas turbine engines in an environment contaminated with volcanic ash. *J*. *Turbomach*. 134 (2012) 051001. DOI:10.1115/1.4006236.

25. J. Kim, M. G. Dunn, A. J. Baran, D. P. Wade, E. L. Tremba. Deposition of volcanic materials in the hot sections of two gas turbine engines. *J*. *Eng*. *Gas Turbines Power* 115 (1993) 641–651. DOI:10.1115/1.2906754.

26. M. Shinozaki, K. A. Roberts, B. van de Goor, T. W. Clyne. Deposition of ingested volcanic ash on *surfaces* in the turbine of a small jet engine. *Adv*. *Eng*. *Mater*. 15 (2013) 986–994. DOI:10.1002/adem.201200357.

27. R. Naraparaju, H. Lau, M. Lange, C. Fischer, D. Kramer, U. Schulz, K. Weber. Integrated testing approach using a customized micro turbine for a volcanic ash and CMAS related degradation study of thermal barrier coatings. *Surf*. *Coat Tech*. 337 (2018) 198–208. DOI: 10.1016/j.surfcoat.2018.01.030.

28. C. Verdy, C. Coddet, G. Montavon, M. Molière, M. Vierling, D. Sokolov. Physics and chemistry of ash in gas turbines: the HVOF technique as a powerful simulation tool. ASME Turbo Expo 2012: Turbine Technical Conference and Exposition, Copenhagen, Denmark. 44670 (2012) 529–534. DOI: 10.1115/GT2012-68275.

29. C. Taltavull, J. Dean, T. W. Clyne. Adhesion of volcanic ash particles under controlled conditions and implications for their deposition in gas turbines. *Adv*. *Eng*. *Mater*. 18 (2016) 803–813. DOI:10.1002/adem.201500371.

30. J. Dean, C. Taltavull, T. W. Clyne. Influence of the composition and viscosity of volcanic ashes on their adhesion within gas turbine aeroengines. *Acta Mater*. 109 (2016) 8–16. DOI: 10.1016/j.actamat.2016.02.011

31. C. Giehl, R. A. Brooker, H. Marxer, M. Nowak. An experimental simulation of volcanic ash *deposition* in gas turbines and implications for jet engine safety. *Chem*. *Geol*. 461 (2017) 160–170. DOI:10.1016/j.chemgeo.2016.11.024.

32. H. N., Webster, D. J. Thomson, B. T. Johnson, I. P. C. Heard, K. Turnbull, F. Marenco, N. I. Kristiansen, J. Dorsey, A. Minikin, B. Weinzierl, U. Schumann, R. S. J. Sparks, S. C. Loughlin, M. C. Hort, S. J. Leadbetter, B. J. Devenish, A. J. Manning, C. S. Witham, J. M. Haywood, B. W. Golding. Operational prediction of ash concentrations in the distal volcanic cloud from the 2010 Eyjafjallajökull eruption. *J*. *Geophys*. *Res*. *Atmos*. 117 (2012) D00U08. DOI:10.1029/2011JD016790.

33. D. Giordano, J. K. Russell, D. B. Dingwell. Viscosity of magmatic liquids: a model. *Earth Planet Sci*. *Lett*. 271 (2008) 123–134. DOI: 10.1016/j.epsl.2008.03.038.

34. W. Song, Y. Lavallée, F. B. Wadsworth, K. U. Hess, D. B. Dingwell. Wetting and spreading of molten volcanic ash in jet engines. *J*. *Phys*. *Chem*. *Lett*. 8 (2017) 1878–1884. DOI: 10.1021/acs.jpclett.7b00417.

35. Y. Tanaka, F. Fukumoto. Investigation of dominating factors on flattening behavior of plasma sprayed ceramic particles. *Surf*. *Coat*. *Technol*. 120–121 (1999) 124–130. DOI:10.1016/S0257-8972(99)00348-5.

36. G. Mauer, R. Vaßen, S. Zimmermann, T. Biermordt, M. Heinrich, J. L. Marques, K. Landes, J. Schein. Investigation and comparison of in-flight particle velocity during the plasma-spray process as measured by

laser doppler anemometry and DPV-2000. *J. Therm. Spray Technol.* 22 (2013) 892–900. DOI:10.1007/s11666-013-9940-9.

37. M. Georg, R. Vaßen, D. Stöver. Plasma and particle temperature measurements in thermal spray: approaches and applications. *J. Therm. Spray Technol.* 20 (2011) 391–406. DOI: 10.1007/s11666-010-9603-z.

38. K. Shinoda, T. Koseki, T. Yoshida. Influence of impact parameters of zirconia droplets on splat formation and morphology in plasma spraying. *J. Appl. Phys.* 100 (2006) 074903. DOI: 10.1063/1.2355446.

39. R. J. Clarkson, E. J. E. Majewicz, P. Mack. A re-evaluation of the 2010 quantitative understanding of the effects volcanic ash has on gas turbine engines. *Proc. Inst. Mechanical Eng. G.* 230 (2016) 2274–2291. DOI: 10.1177/0954410015623372.

40. H. L. Tanaka, M. Iguchi. Numerical simulation of volcanic ash plume dispersal from kuchinoerabujima on 29 May 2015. *J. Nat. Disaster Sci.* 37 (2016) 79–90. DOI: 10.1177/0954410015623372.

41. A. Vogel, A. J. Durant, M. Cassiani, R. J. Clarkson, M. Slaby, S. Diplas, K. Krüger, A. Stohl. Simulation of volcanic ash ingestion into a large aero engine: Particle-fan interactions. *J. Turbomach.* 141 (2019) 011010. DOI:10.1115/1.4041464.

42. T. Bose. Airbreathing propulsion: An introduction. Springer New York, 2012, pp. 27–86.

43. P. Patricio, J. M. Tavares. Simple thermodynamics of jet engines. *Am. J. Phys.* 78 (2018) 809−814. *DOI*: 10.1119/1.3373924.

44. W. Balicki, P. Glowacki, S. Szczecinski, R. Chachurski, J. Szczeciński. Effect of the atmosphere on the performances of aviation turbine engines. *Acta Mech. Autom.* 8 (2014) 70−73. DOI: 10.2478/ama-2014-0012.

45. N. K. Rizk, H. C. Mongia. Three-dimensional analysis of gas turbine combustors. *J. Propul. Power* 7 (1991) 445−451. DOI: 10.2514/3.23346.

46. H. Wang, R. B. Dinwiddie. Characterization of thermal barrier coatings using thermal methods. *Adv. Eng. Mater.* 3 (2001) 465−468.

47. https://accuratus.com/alumox.html

48. M. A. Mulero, J. Zapata, R. Vilar, V. Martínez, R. Gadow. Automated image inspection system to quantify thermal spray splat morphology. *Surf. Coat. Technol.* 278 (2015) 1−11. DOI: 10.1016/j.surfcoat.2015.07.065.

49. C. A. Schneider, W. S. Rasband, K. W. Eliceiri. NIH Image to Image J: 25 years of image analysis. *Nat. Methods.* 9 (2012) 671–675. DOI: 10.1038/nmeth.2089.

50. Yarin, A. L. Drop impact dynamics: splashing, spreading, receding, bouncing. *Annu. Rev. Fluid Mech.* 38 (2006) 159–192. DOI: 10.1146/annurev.fluid.38.050304.092144.

51. S. Goutier, M. Vardelle, P. Fauchais. Comparison between metallic and ceramic splats: Influence of viscosity and kinetic energy on the particle flattening. *Surf. Coat. Technol.* 235 (2013) 657–668.

52. W. Song, L. Tang, X. Zhu, Y. Wu, Y. Rong, Z. Zhu, S. Koyama. Fusibility and flow properties of coal ash and slag. Fuel 88 (2009) 297–304. DOI: 10.1016/j.fuel.2008.09.015

53. S. Chandra, P. Fauchais. Formation of solid splats during thermal spray deposition. *J. Therm. Spray Technol.* 18 (2009) 148–180. DOI: 10.1007/s11666-009-9294-5.

54. S. Schiaffino, A. A. Sonin. Molten droplet deposition and solidification at low Weber numbers. *Phys. Fluids.* 9 (1997) 3172–3187. DOI: 10.1063/1.869434.

55. C. W. Kang, H. W. Ng. Splat morphology and spreading behavior due to oblique impact of droplets onto substrates in plasma spray coating process. *Surf. Coat. Technol.* 200 (2006) 5462–5477. DOI:10.1016/j.surfcoat.2005.07.067.

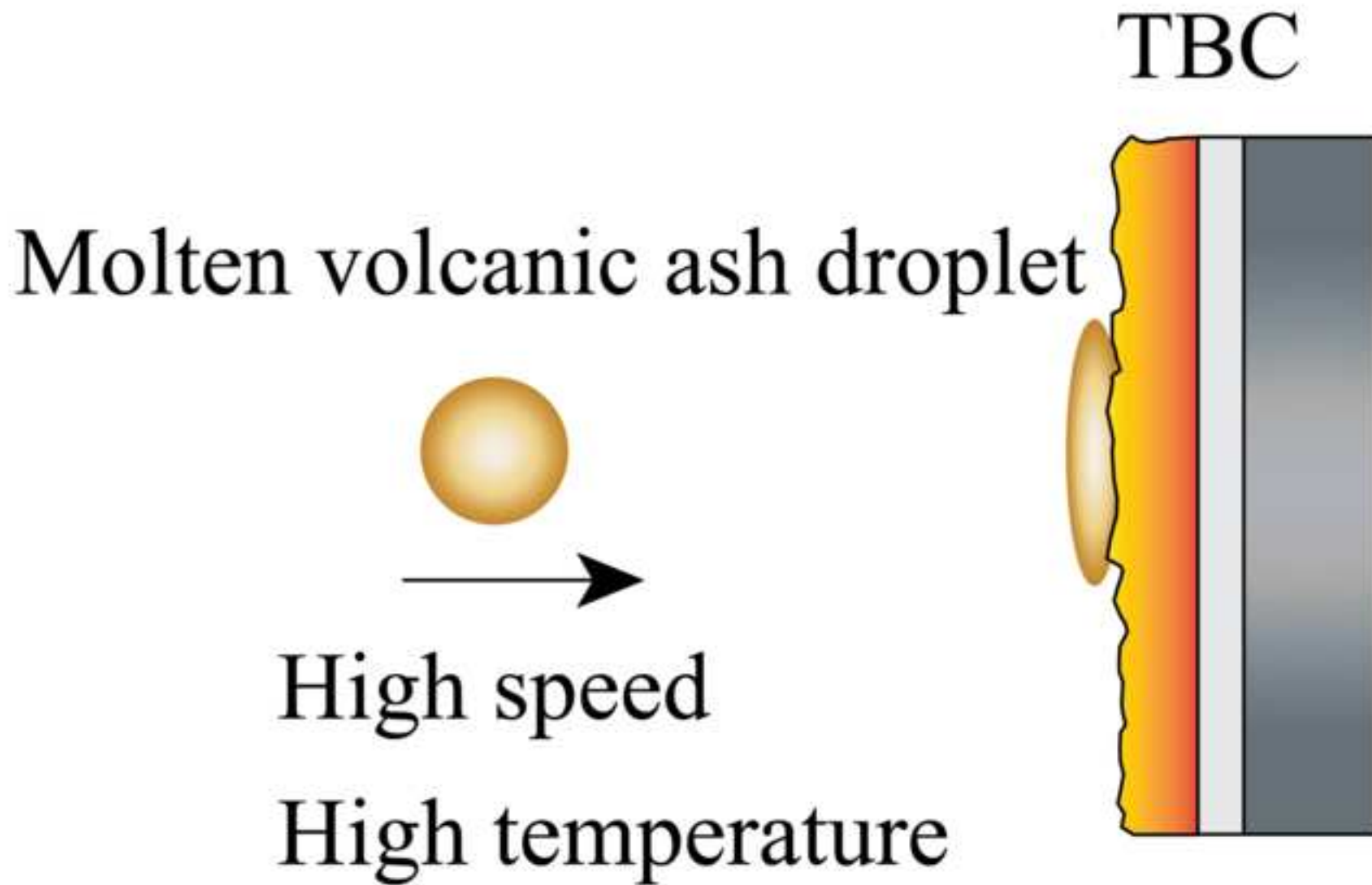56. H. Zhang, X. Y. Wang, L. L. Zheng, X. Y. Jiang. Studies of splat morphology and rapid solidification during thermal spraying. *Int. J. Heat. Mass. Transf.* 44 (2001) 4579–4592. DOI:10.1016/S0017-9310(01)00109-0.

57. M. A. Mulero, J. Zapata, R. Vilar, V. Martínez, R. Gadow. Automated image inspection system to quantify thermal spray splat morphology. *Surf. Coat. Technol.* 278 (2015) 1–11. DOI:10.1016/j.surfcoat.2015.07.065.

58. L. Sadowski, S. Czarnecki, J. Hola. Evaluation of the height 3D roughness parameters of concrete substrate and the adhesion to epoxy resin. *Int. J. Adhes. Adhes.* 67 (2016) 3–13. DOI:10.1016/j.ijadhadh.2015.12.019.

59. S. Goutier, M. Vardelle, P. Fauchais. Comparison between metallic and ceramic splats: Influence of viscosity and kinetic energy on the particle flattening. *Surf. Coat. Technol.* 235 (2013) 657–668. DOI: 10.1016/j.surfcoat.2013.08.044.

Impact interaction of in-flight high-energy molten volcanic ash droplets with jet engines

Wenjia Song [a,b] [*], Shanjie Yang [a,c], Masahiro Fukumoto [d], Yan Lavallée [e], Siddharth Lokachari [a], Hongbo Guo [c], Yancheng You [b] [*], Donald B. Dingwell [a]

[a] Department of Earth and Environmental Sciences, Ludwig-Maximilians Universität München, Theresienstrasse 41, 80333 Munich, Germany

[b] School of Aerospace Engineering, Xiamen University, 361102 Xiamen, China

[c] School of Materials Science and Engineering, Beihang University, 100191 Beijing, China

[d] Department of Mechanical Engineering, Toyohashi University of Technology, 1-1 Tempaku-cho, 441-8580 Toyohashi, Japan

[e] Department of Earth, Ocean and Ecological Sciences, University of Liverpool, Liverpool L69 3GP, UK

*Corresponding authors:

Wenjia Song, Department of Earth and Environmental Sciences, Ludwig-Maximilians-Universität (LMU), Theresienstrasse 41, 80333 Munich, Germany. (wenjia.song@lmu.de)
Telephone: +49 (0) 89 2180 4293

Yancheng You, School of Aerospace Engineering, Xiamen University, 361102 Xiamen, China. (yancheng.you@xmu.edu.cn)
Telephone: +86 (0) 592 2186 849

Supplementary Figure 1 Estimation of the relative contribution of in-flight of the characteristics of high-energy molten volcanic ash droplets to adhesion rate. (a-e) the droplet temperature (a), viscosity (b), concentration (c), diameter (d), and impact velocity (e) as functions of adhesion rate, respectively. (f) The comparison of coefficient of determination (R^2) between these parameters above mentioned and adhesion rate for three kinds of substrates.

Supplementary Table 1 The specific plasma spraying conditions

Operating gas flow (L min⁻¹)	
Ar	40
H_2	4
Arc current (A)	800
Arc voltage (V)	70
Spray distance (mm)	50, 75, 100, 125
Powder feed rate (g min⁻¹)	0.8

Supplementary Table 2 Descriptive statistics for the morphology of single splats deposited on APS TBCs, EB-PVD TBCs, and Al_2O_3 substrates during impact experiments conducted at torch distance of 100 mm

Substrate	N	Area (μm⁻²) mean	s.e.m.	Perimeter (μm) mean	s.e.m.	Circularity mean	s.e.m.
APS TBCs	76	210.60	49.66	44.14	4.91	0.808	0.015
EB-PVD TBCs	55	330.75	146.50	58.88	13.92	0.797	0.022
Al_2O_3	48	244.08	104.21	78.76	22.37	0.525	0.040

Supplementary Table 3 Descriptive statistics for the morphology of single splats deposited on Al_2O_3 substrates during impact experiments conducted at torch distances between 50 mm and 125 mm

Distance (mm)	N	Area (μm^{-2}) mean	s.e.m.	Perimeter (μm) mean	s.e.m.	Circularity mean	s.e.m.
50	1354	168.29	9.13	47.50	1.41	0.795	0.005
75	561	232.72	21.67	86.16	4.22	0.428	0.010
100	437	346.81	33.64	97.53	4.95	0.448	0.012
125	301	87.46	10.44	39.83	2.20	0.638	0.013

Supplementary Table 4 Absolute weights of APS TBCs, EB-PVD TBCs and Al_2O_3 substrate before and after deposition experiments at various distances

Distance (mm)	APS TBCs Before (g)	After (g)	EB-PVD TBCs Before (g)	After (g)	Al_2O_3 substrate Before (g)	After (g)
50	0.8454	0.8507	0.9145	0.9179	21.2130	21.2530
75	0.8567	0.8558	0.9277	0.9547	21.2100	21.2380
100	0.8805	0.8815	0.9081	0.9091	21.2360	21.2520
125	0.9456	0.9466	0.9340	0.9343	21.2150	21.2220

Supplementary Table 5 Descriptive statistics for the characteristics of in-flight molten volcanic ash droplets prior to impact

Distance (mm)		50	75	100	125
Number of droplets monitored, N		5,000	4,999	3,652	3,108
Temperature (ºC)	Max.	3,999	3,824	3,144	2,875
	Min.	1,759	1,728	1,649	1,543
	mean	2,543	2,450	2,367	2,198
	s.e.m.	3.38	2.86	2.98	3.16
Velocity (m s^{-1})	Max.	498	470	403	313
	Min.	45	39	49	60
	mean	231	262	244	199
	s.e.m.	0.70	0.70	0.69	0.57
Diameter (μm)	Max.	89	91	110	108
	Min.	3	4	7	8
	mean	21	20	23	29
	s.e.m.	0.14	0.13	0.21	0.23
Weber number (We)	Max.	21371	29300	24651	21792
	Min.	194	180	176	426
	mean	6100	7854	7626	6415
	s.e.m.	41.37	54.16	62.18	54.88
Reynolds number (Re)	Max.	6.09×10^{12}	4.9×10^{5}	2.64×10^{8}	5.42×10^{6}
	Min.	19.97	6.29×10^{4}	5.71	1.34
	mean	4.04×10^{9}	1.33×10^{4}	2.59×10^{5}	20122
	s.e.m.	1.97×10^{9}	929.13	7.42×10^{4}	2.1×10^{3}

Supplementary Table 6 Multivariate linear regression analyses for the relationship between the morphology of molten volcanic ash splats on various substrates and characteristics of in-flight droplet prior to impact

Multiple linear curve regression parameters			
Coefficients ± SE		Y-axis intercept ± SE	Correlation coefficient, R^2
Log We	*Log Re*		
-2.10 ± 0.09	0.009 ± 0.002	7.79 ± 0.35	0.999

Supplementary Table 7 Linear regression parameters for the adhesion rate, ε, of in-flight molten volcanic ash droplet from deposition experiments conducted at torch distances between 50 mm and 125 mm compared to the substrate roughness parameter, S_a, corresponding to APS TBCs, EB-PVD TBCs, and Al_2O_3 substrate in Fig. 14b

Distance (mm)	Linear curve regression parameters		
	Slope ± SE	Y-axis intercept ± SE	Correlation coefficient, R^2
50	0.076 ± 0.01	0.149 ± 0.04	0.979
75	0.052 ± 0.01	0.105 ± 0.03	0.978
100	0.016 ± 0.002	0.067 ± 0.01	0.977
125	0.003 ± 0.0001	0.029 ± 0.0004	0.999

Supplementary Table 8 Linear regression parameters for the adhesion rate, ε, of in-flight molten volcanic ash droplets on APS TBCs, EB-PVD TBCs, and Al_2O_3 substrate with compared to the dimensionless parameter, δ in Fig. 14c

Substrate	Linear curve regression parameters		
	Slope ± SE	Y-axis intercept ± SE	Correlation coefficient, R^2
APS TBCs	-1.10 ± 0.09	-1.77 ± 0.09	0.988
EB-PVD TBCs	-0.99 ± 0.08	-1.71 ± 0.08	0.986
Al_2O_3	-0.78 ± 0.05	-1.38 ± 0.03	0.993